REPORT DOCUMENTATION PAGE

1. REPORT DATE	2. REPORT TYPE Professional Paper	3. DATES COVERED

4. TITLE AND SUBTITLE Experimental and Numerical Investigation of Vortex Shedding of a Representative UCAV Configuration for Vortex Flow Control	5a. CONTRACT NUMBER
	5b. GRANT NUMBER
	5c. PROGRAM ELEMENT NUMBER

6. AUTHOR(S) Terence Ghee; Doug Hall	5d. PROJECT NUMBER
	5e. TASK NUMBER
	5f. WORK UNIT NUMBER

7. PERFORMING ORGANIZATION NAME(S) AND ADDRESS(ES) Naval Air Warfare Center Aircraft Division 22347 Cedar Point Road, Unit #6 Patuxent River, Maryland 20670-1161	8. PERFORMING ORGANIZATION REPORT NUMBER

9. SPONSORING/MONITORING AGENCY NAME(S) AND ADDRESS(ES)	10. SPONSOR/MONITOR'S ACRONYM(S)
	11. SPONSOR/MONITOR'S REPORT NUMBER(S)

12. DISTRIBUTION/AVAILABILITY STATEMENT

Approved for public release; distribution is unlimited.

13. SUPPLEMENTARY NOTES

14. ABSTRACT

A 4% Uninhabited Combat Air Vehicle (UCAV) has been extensively tested at low speeds in a wind tunnel to investigate using vortex flow control to control vehicle attitude. The program is the initial step to utilize experimental and computational techniques to understand the flowfield environment on a representative low-observable air vehicle and use that understanding to apply an efficient vortex flow control apparatus. Gross flow field characteristics were identified using flow visualization and the approximate vortex location was determined for a number of angles-of-attack for a tunnel dynamic pressure of 26.47 psf. From this study, the model was instrumented with pressure transducers at appropriate locations on the wing and unsteady data was acquired for a number of angles-of-attack and tunnel dynamic pressures. A limited hot-wire anemometry study was also conducted. A six-component internal balance was then installed to measure aerodynamic forces and moments. Limited steady electronically scanned pressure data was acquired. Computational fluid dynamic (CFD) analysis was conducted on the model geometry to compare with the results from the wind tunnel study. The results show two vortex structures: a weak apex vortex and a stronger wing vortex. Wing vortex frequency exhibits a rather broad-banded dominant frequency between 6 and 11 Strouhal number. Maximum suction pressure was seen to move forward on the wing leading edge with increasing angle-of-attack. The CFD poorly predicted the physical behavior of the vortex.

15. SUBJECT TERMS

Vortex; Uninhabited Combat Air Vehicle (UCAV)

16. SECURITY CLASSIFICATION OF:			17. LIMITATION OF ABSTRACT	18. NUMBER OF PAGES	19a. NAME OF RESPONSIBLE PERSON Terence Ghee / Doug Hall
a. REPORT	b. ABSTRACT	c. THIS PAGE			19b. TELEPHONE NUMBER (include area code)
		Unclassified		15	(301) 342-8536 / (301) 342-8534

20010824 084

Experimental and Numerical Investigation of Vortex Shedding of a Representative UCAV Configuration for Vortex Flow Control

Terence A. Ghee [*], Doug R. Hall [†]
NAVAIR, Code 4321
Bldg. 2187, Suite 1320B
Patuxent River, MD 20670-1906
USA

ABSTRACT

A 4% Uninhabited Combat Air Vehicle (UCAV) has been extensively tested at low speeds in a wind tunnel to investigate using vortex flow control to control vehicle attitude. The program is the initial step to utilize experimental and computational techniques to understand the flowfield environment on a representative low-observable air vehicle and use that understanding to apply an efficient vortex flow control apparatus. Gross flow field characteristics were identified using flow visualization and the approximate vortex location was determined for a number of angles-of-attack for a tunnel dynamic pressure of 26.74 psf. From this study, the model was instrumented with pressure transducers at appropriate locations on the wing and unsteady data was acquired for a number of angles-of-attack and tunnel dynamic pressures. A limited hot-wire anemometry study was also conducted. A six-component internal balance was then installed to measure aerodynamic forces and moments. Limited steady electronically scanned pressure data was acquired. Computational fluid dynamic (CFD) analysis was conducted on the model geometry to compare with the results from the wind tunnel study. The results show two vortex structures: a weak apex vortex and a stronger wing vortex. Wing vortex frequency exhibits a rather broad-banded dominant frequency between 6 and 11 Strouhal number. Maximum suction pressure was seen to move forward on the wing leading edge with increasing angle-of-attack. The CFD results poorly predicted the physical behavior of the vortex.

NOMENCLATURE

b	span, 2.160 ft	Re	Reynolds number, $(\rho_\infty V_\infty MAC)/\mu_\infty$, 0.73E6
MAC	mean aerodynamic chord, 0.765 ft	RMS	root mean square
C	coherence	std	standard deviation
C_P	pressure coefficient, $p-p_\infty/q_\infty$	Se	transducer sensitivity, volt/psi
C_R	root chord, 1.280 ft	S	wing area, 1.210 ft^2
f	frequency, Hz	St	Strouhal number, $(b\ f)/V_\infty$
G	amplifier gain	t	time, sec
I_{raw}	raw integer value (digital)	V	excitation voltage, 10 volt
M_∞	freestream Mach number, V_∞/a_∞, 0.13	V_∞	tunnel freestream velocity, 150 ft/s
P	pressure, psi	α	geometric angle of attack, degree
P_{Ref}	reference pressure, psi	μ_∞	viscosity, 3.7373E-7, slug/(ft sec)
PSD	power spectral density	τ	non-dimensional time, $(t\ a_\infty)/MAC$
q_∞	tunnel dynamic pressure, 26.74 psf		

INTRODUCTION

On vehicles with swept wings, leading edge vortices are created at off-design conditions, Ref. 1. The leading edge vortex generally has a beneficial effect in the form of increased lift at higher angles-of-attack. By controlling the location of the shed vortex or vortices, vehicle roll and pitch control may be possible. Uninhabited Combat Air Vehicles (UCAVs) that utilize stealth to avoid detection suffer a radar signature increase when control surfaces are deflected. Thus, there is an advantage to be gained by limiting flap deflection

_____

* Aerospace Engineer, ph: 301 342 8536 FAX: 301 342 8588, gheeta@navair.navy.mil
† Aerospace Engineer, ph: 301 342 8534, FAX: 301 342 8588, halldr@navair.navy.mil

by utilizing vortex flow control to change vehicle attitude. However, a thorough understanding of the vehicle flowfield is needed to best mate a flow control device to the vehicle. In view of this, an experimental and numerical investigation was conducted on a representative UCAV configuration to define the flowfield and investigate methods to control vortex location, and ultimately, vehicle attitude. The test program was developed in three phases: 1) vortex location identification using laser light sheet flow visualization and fluorescent oil applied to the model surface, 2) vortex quantification through surface and off-body measurements, and 3) vortex manipulation utilizing a simple blowing jet. This paper reports the results of the first two phases of the program.

EXPERIMENTAL SETUP
The tests were conducted in the Naval Aerodynamic Test Facility (NATF) as part of the Naval Air Warfare Center In-House Laboratory Independent Research (ILIR) program. The NATF is a four-foot by four-foot closed test section, open-return wind tunnel. The facility incorporates a 200 horsepower motor that drives a variable pitch fan and delivers a maximum velocity of 205 ft/s. In addition, the facility has honeycomb and three sets of flow conditioning screens that minimize freestream turbulence intensity to approximately 0.15% and freestream velocity differences of 1%. Fig. 1 shows the 4% UCAV model in the NATF
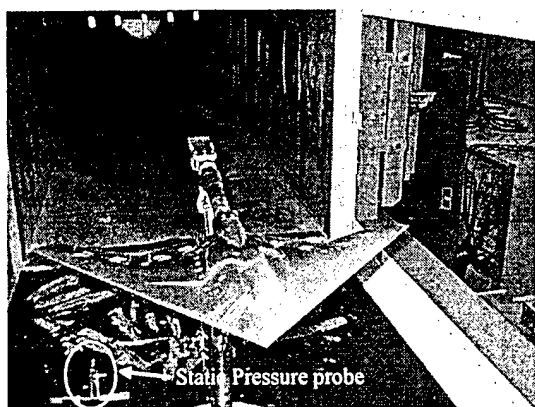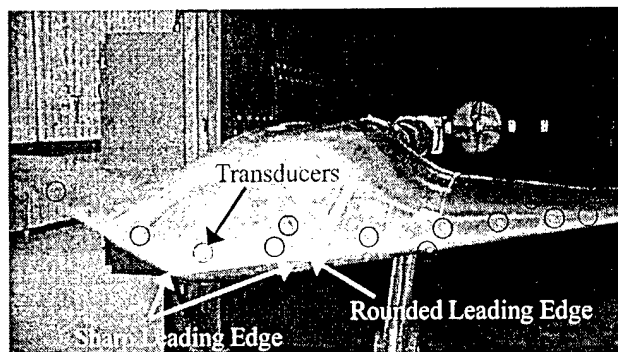

Fig. 1 – 4% UCAV in NATF

Fig. 2 - 4% UCAV Leading Edge

A 4% UCAV model with 47-degree leading edge was used as a representative configuration. The model was fabricated of stainless steel for the US Air Force Research Laboratory and tested previously to assess aerodynamic performance, Ref. 2. The leading edge of the cranked-delta-wing vehicle has a sharp chine at the nose that transitions to round in the vicinity of the wing/body juncture, see Fig. 2. Also visible in Fig. 2 and detailed in Fig. 3, are the 13 Kulite fast-response, differential gage, pressure transducers installed on the model. An inlet nose plug was installed for the majority of the testing to create a more simplified geometry with out the added complexity of a flow-through duct. In addition, transducer signal/power cables could be run through the duct work, thus avoiding expensive machining of the model. The nose/propulsion inlet plug also allows the testing of novel vortex flow control devices, affixed to the plug, to be easily fabricated and evaluated.

A sting assembly attached to the facility pitch strut supported the model and the support system was constrained vertically; the model moved off-centerline with changing angle-of-attack. . Angle-of-attack was measured at model support system using an Allied Signal QA-2000 accelerometer. The model was set to 0.108 degrees in yaw to correct cross flow angularity.

The unsteady pressure data was acquired using a 32-channel, 14-bit DSP Technology, Inc. IMPAX unsteady data acquisition system connected to a personal computer. This system acquired the data simultaneously and thus the data was coincident.
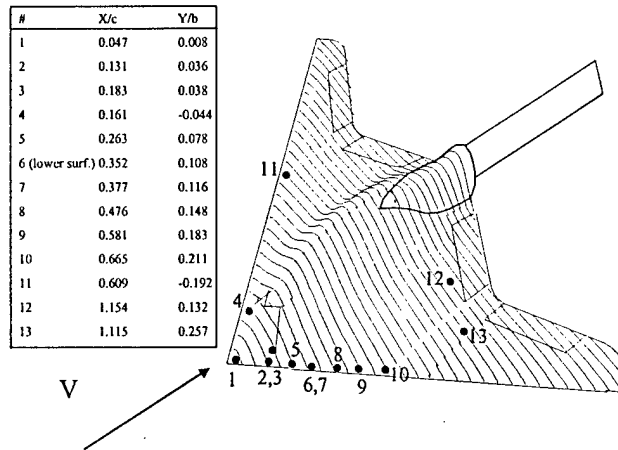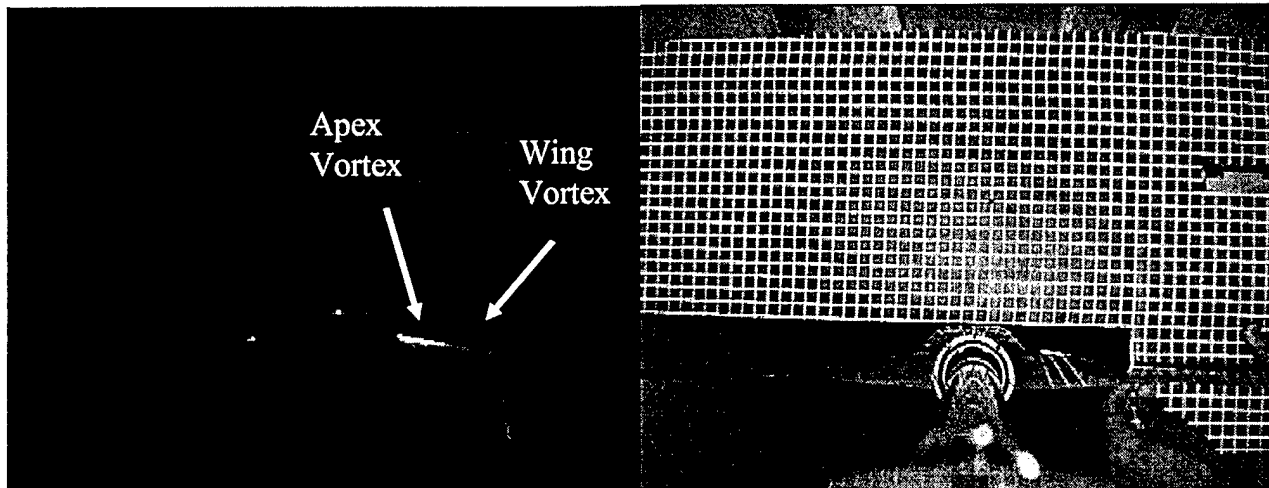
#	X/c	Y/b
1	0.047	0.008
2	0.131	0.036
3	0.183	0.038
4	0.161	-0.044
5	0.263	0.078
6 (lower surf.)	0.352	0.108
7	0.377	0.116
8	0.476	0.148
9	0.581	0.183
10	0.665	0.211
11	0.609	-0.192
12	1.154	0.132
13	1.115	0.257

Fig. 3 – Transducer Location

a) Video data, view looking upstream.

b) Reference grid video, used to quantify vortex location.

Fig. 4 – Vortex Location Using Laser Light Sheet, x/MAC = 0.735

PROCEDURE AND DATA REDUCTION
PHASE 1
A flow visualization study was conducted utilizing laser light sheet and injected vaporized propylene glycol to seed the flow. A miniature camera was mounted to the support system sting and orthogonal to the light sheet. To quantify the location of the vortices in space, video data was acquired at a tunnel dynamic pressure of 26.74 psf and at angles-of-attack from 6 to 14 degrees in increments of 2 degrees. After tunnel shutdown, a reference grid was placed in the plane of the light sheet. See Fig. 4 for an example of video data and the reference grid. Using a known reference location on the grid and digital image processing techniques, the vortex locations were determined. In addition, fluorescent oil flow visualization studies were conducted at an angle-of-attack of 10 degrees and for wind tunnel velocities of 75 ft/s, 100 ft/s, 125 ft/s, and 150 ft/s, see Fig. 5. Note, Fig. 5 has been digitally enhanced for clarity. Both of these studies were performed utilizing a dummy balance. This allowed

angular deformations to be minimized. The results from this phase were used to guide transducer placement on the model.
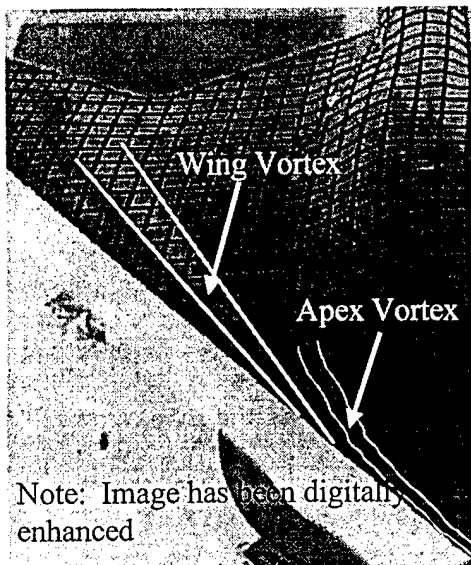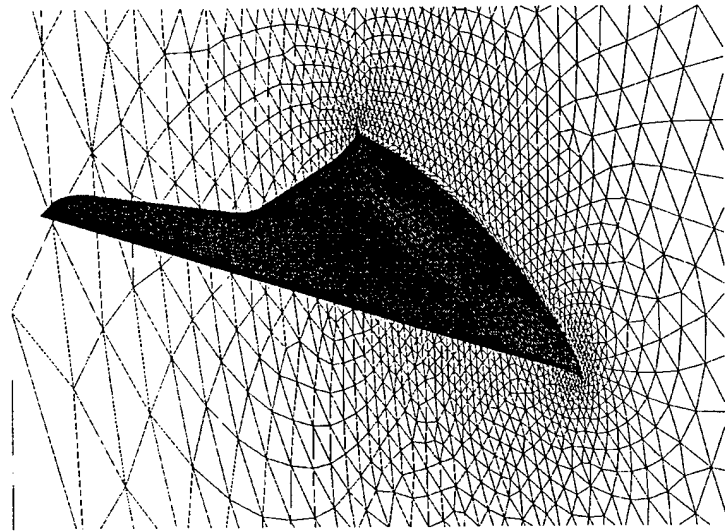

Fig. 5 – Oil Flow at 10 Degrees Angle-of-Attack

Fig. 6 – CFD Grid

PHASE 2

The unsteady pressure tests were generally conducted at a constant tunnel velocity of 150 ft/s (q_∞=26.74 psf and Reynolds number of 0.73 million based on MAC). Model incidence was varied from 0 degrees to 18 degrees in increments of 1 degree for the unsteady pressure portion of the testing. Thirty seconds of wind-off-zero data were acquired previous to tunnel start up. The tunnel was driven to 150 ft/s and after test conditions steadied, unsteady pressure data was acquired. Unsteady pressures were sampled at 10,000 samples/second for 30 seconds. A Butterworth 8-pole filter provided a low-pass cut off frequency of 2,000 Hz. Following tunnel shutdown, wind-off-zero data were acquired for comparison to the pre-test wind-off-zero data. The data was analyzed to determine the time-history and PSD characteristics. The large size of the data array (307200 samples per transducer per run) necessitated the data be analyzed on a high performance computer system. Matlab software was used to determine the pressure time history and pressure power spectral density (PSD) using an SGI Octane computer workstation. The data was converted to engineering units using the appropriate gains and sensitivities. The assumption was made that the wind-off-zero pressure was essentially total pressure. At the time of the test, a barometric pressure device was not available. Thus, tunnel static pressure was determined by subtracting the tunnel dynamic pressure from the wind-off-zero (or total) pressure. Pressure coefficient data were determined by the following:

$$C_P = \frac{(P_{measured} - P_{wind\text{-}off\,zero}) - P_\infty}{(q_\infty)}$$

The coherent acoustic noise present in the freestream data was removed from the pressure measurements by using an unsteady static pressure probe located on the tunnel floor, see Fig. 1. The coherence was a function of the power spectrum of the freestream noise and the power spectrum of the data at an arbitrary angle-of-attack and the cross spectrum of the freestream noise and the data at the arbitrary angle-of-attack, see Refs. 3 and 4. Thus, the coherence was found by:

$$C = \frac{(PSD_{Ref., meas})^2}{(PSD_{Ref.,Ref.}) * (PSD_{meas, meas})}$$

4

The PSD of the measured data is then:

$$PSD_{meas} = (1 - C) * PSD_{meas,\ uncorrected} \qquad (RMS^2)$$

The algorithm to determine the PSD was based on the method by Welch, Ref. 5. The data were segmented into windows to allow thirty averages and corresponded to a frequency resolution of 1 Hz. No data overlapping was employed and a Hanning filter was used with a window length the same size as the data segments. The mean was eliminated from the PSD and coherence calculations and a 95% confidence criteria was used to gage the PSD assessment.

Limited hot-wire anemometry data was acquired at a tunnel dynamic pressure of 26.74 psf and at x/MAC of 0.55 and 0.58 for angles-of-attack of 8 and 10 degrees, respectively. A horizontal traverse was accomplished extending from 0.08 to 0.21 y/b. 1024 samples of data was acquired at a sample rate of 50,000 samples/second with a 20,000 low pass filter (the data was also sent to the unsteady data system and recorded at the same settings as the pressure data quoted previously). This data was of limited value as the longitudinal location of the probe was not far enough downstream to capture the dynamic flowfield of the vortex. Unsteady pressure and hot-wire anemometry data incorporated the dummy balance.

Force and moment testing was accomplished on the model. A Modern Machine UT-37BN six-component balance replaced the dummy balance used in the previous studies. Table 1 provides details of the maximum full-scale loads and error report. Limited electronically scanned pressure (ESP) data was obtained. This provided some wing pressures and quantified base pressure for aerodynamic force correction. The data was corrected for downwash, solid and wake blockage (using an iterative Maskell scheme), base pressure, and sting bending.

Table 1 - Balance Uncertainty

% FS - Calibration Plus Proof Loads

	NF	AF	PM	RM	YM	SF	C_L @ 200 ft/s	C_D @ 200 ft/s
Maximum	0.12	0.81	0.14	0.22	0.16	0.07	0.0071	0.0048
Minimum	-0.07	-0.3	-0.12	-0.32	-0.2	-0.07		
FS Load	300 lb	30 lb	1,000 in-lb	150 in-lb	500 in-lb	200 lb		

The CFD calculations were performed using the COBALT code, a time-accurate, unstructured Navier-Stokes solver, see Refs.6 and 7. Cobalt solves the Navier-Stokes equations using a Riemann method. Implicit solutions are obtained on unstructured, cell centered, finite volume cells. The cell type is arbitrary. The volume grid consists of one zone that is subdivided for parallel processing. The grid model utilized a symmetry plane for the model and consisted of 381,000 cells, see Fig. 6. The solution was obtained at time step of 1/40,000 second.

ERROR ANALYSIS
An uncertainty estimate of the data was undertaken to gage the accuracy of the test results. The unsteady pressure measurement accuracy was dictated by the quoted instrumentation repeatability of 0.1%. The effect of the accuracy of the A/D system and power supply was evaluated and found to be negligible on the data accuracy (however, these uncertainties were incorporated in the error analysis). The tunnel velocity varied in the test section by approximately 1% and fluctuated by approximately 0.75% at the tested tunnel velocity. Using a method outlined in Ref. 8, the uncertainty in pressure coefficient was estimated to be 0.027. The highest and lowest resolvable frequencies were 2000 Hz and 0.03 Hz, respectively. These values were based on the use of a low-pass filter (the Nyquist criteria would dictate the highest frequency of 4,267 Hz) and dwell time. The frequency that could be resolved in the PSD was approximately 1Hz. Table 1 provides estimates of the error associated with the balance data at a tunnel dynamic pressure of 26.74 psf.

RESULTS
The force and moment coefficients are presented in Fig. 7 for a tunnel dynamic pressure of 26.74 psf. A noticeable lift break is seen in Fig. 7a at an angle-of-attack of three degrees. This is indicative of the transition

from attached flow to leading edge vortex separation. Drag Coefficient data appears ragged around C_{Dmin} most likely due to balance insensitivity.

From both CFD and Phase 1 experiments, two distinct vortex systems were found: one vortex emanating from the nose of the vehicle and a second vortex issuing from the wing leading edge, see Fig. 8. CFD analyses, showed good agreement in the basic flow structure. The wing vortex was found to emanate at the transition from a sharp to rounded leading edge. Laser light sheet images were analyzed and the vortex location in space was quantified for an angle-of-attack of 12 degrees, see Fig. 9a. Using fluorescent oil flow visualization, the wing vortex was found to emanate from the leading edge at an approximate location of x/MAC=0.279 and y/b/2=0.184. Also plotted on Fig. 9a and 9b, are the transducer locations for the starboard and port side of the wing. The port vortex location data is fictitious and assumes vortex symmetry.

The results from the flow visualization studies were used to guide transducer placement. Unsteady pressure data was analyzed and plotted for the mean and standard deviation of the pressure coefficient versus angle-of-attack, see Figs. 10 and 11. The mean pressure coefficient is an indication of the approximate vortex location along the leading edge. As angle-of-attack increases, the vortex was seen to move more inboard as evidenced in Fig. 10 by increase in suction pressure toward the apex as angle-of-attack increases. The flowfield appears to be asymmetric as evidenced by Transducer pairs 10 and 11 having different pressure characteristics.

To a certain extent, the standard deviation of the pressure coefficient is a measure of the flow unsteadiness, see Fig. 11. However, the maximum standard deviation was seen to occur at a higher angle-of-attack than the maximum suction peak. Transducer 4 experiences a rapid rise in standard deviation at higher angles-of-attack and is most likely indicative of separation.

PSD plots for Transducer 8 as a series of increasing angle-of-attack is presented in Fig. 12. . This location was chosen because it generally was the first to exhibit a defined vortex frequency spectrum.

At an angle-of-attack of 8 degrees, the only detectable frequency spikes were due to the wind tunnel fan. This

	Table 2 - Maximum Strouhal Number					
α	Transducer 8	Transducer 9	Transducer 10	Transducer 11	Transducer 12	Transducer 13
12	10.1567	10.1348		7.0207		
13	8.7247	10.3698	9.0184	8.7247	5.8456	
14	7.0795	10.1348	8.6071	11.0161		
15	6.5507	8.7834	7.9608	10.5461		
16	8.1371	7.4908		8.6071	1.909	5.023
17	8.1959	8.2546		9.5472	1.909	4.9643
18					1.7915	3.3191

location along the leading edge was found to have a defined vortex frequency. This figure is typical for transducers nearer the apex and at low to moderate angles-of-attack. As the angle-of-attack is increased, a broad band frequency spike develops. The maximum of this spectrum varies as shown in Table 2:

The corresponding pressure coefficient time histories for Transducer 8 are shown in Fig. 13. Non-dimensional time is plotted for the equivalent of 0.2 seconds. A low frequency pulse is seen at an angle-of-attack of 16 degrees. This pulse was seen at the same angle-of-attack in Fig. 12 as a large spike at a Strouhal number of 0.5.

Table 3 - CFD comparison with experiment for mean and standard deviation of pressure coefficient											
Cp Mean											
Transducer	1	2	3	5	6	7	8	9	10	12	13
Experiment	-0.2804	-0.528	-0.4712	-1.5909	0.4118	-2.0539	-2.9637	-1.4218	-2.4665	-1.0385	-0.4711
CFD	-0.0696	0.4126	-0.2881	-0.7308	0.4036	-1.0255	-1.4158	-0.0004	-1.6323	-0.1762	-0.5220
Cp Standard Deviation											
Transducer	1	2	3	5	6	7	8	9	10	12	13
Experiment	0.0181	0.0211	0.0188	0.0394	0.0107	0.0372	0.0959	0.0958	0.0875	0.1343	0.0213
CFD	0.0044	0.0023	0.0102	0.0154	0.0138	0.0112	0.0095	0.0002	0.0276	0.0047	0.0047

The low frequency pulse also explains the maximum standard deviation seen in Fig. 11 for this transducer.

CFD calculations show a poor prediction of the pressure and PSD on the model for Transducer 8, see Figs.14a and b. This is most likely due to the lack of grid density in the vicinity of interest. Additional calculations are to include a refined grid in this region of the flow. For the CFD data, the angle-of-attack was set to 12 degrees and the freestream velocity was set to 150 ft/s. The experimental data, the angle-of-attack was 10 degrees and a freestream velocity of 150 ft/s. The difference in angle-of-attack was due to the effect of wind tunnel and sting bending corrections. A study was conducted to determine the effect of angle-of-attack was on the pressure coefficient data. For the range from 9 degrees to 12 degrees angle-of attack, the experimental pressure coefficient was seen to vary less than the difference between experimental and calculated data.
A PSD comparison of the experimental data with the CFD prediction is shown in Fig. 14a. In general, CFD performs rather poorly in predicting the amplitude of the signal. However, the frequency content prediction approximates the experimental data, but is not stellar. Part of the reason for the failure of CFD to predict the experimental data is the limited amount of CFD data available. As reported previously, an artificially limited amount of data was recorded from the CFD prediction. This limited amount of data has been found to violate the Nyquist criteria for the higher significant frequencies found in the experimental data. The CFD predictions are currently being re-run to obtain all the data calculated and thus will have a sample rate of 10,000 samples/second.

In addition to the surface pressure measurements, off-body flow field measurements were undertaken using a hot wire anemometer system mounted on a traverse, see Fig.15. The grid was located at x/MAC = 0.58621 and 0.5521 for surveys at an angle-of-attack of 8 and 10 degrees, respectively. The height above the MAC was determined to be z/MAC = 0.1392 and 0.2073 at an angle-of-attack of 8 and 10 degrees, respectively. The grid resolution of the data was 1/4 inch (y/b =0.010). In Fig. 15, the data is seen to decrease with increasing y/b location. The vehicle leading edge is approximately 0.13 y/b. Little indication of vortex flow is seen. A PSD of the data showed little dynamic frequencies other than those associated with the wind tunnel fan. Most likely, the probe would have to be positioned farther downstream to measure the wing vortex.

One of the original ideas at the outset of the program was to utilize apex blowing to facilitate vortex flow control. This may be attempted, but given the fact of a weak apex vortex that is distinct from the wing vortex and little flow dynamic frequency content, repositioning the apex vortex through steady or pulsed blowing appears unlikely to affect the wing vortex. It may be possible to utilize tangential leading edge blowing on the nose plug to initiate the wing vortex and that may be an avenue to explore. The use of leading edge micro-vortex generators may be effective and will be researched this year. The cost to the low observable signature remains to be determined.

CONCLUSIONS
A comprehensive test program was accomplished to determine the flowfield characterisitcs of a representative UCAV configuration. The tests were conducted in the US Navy NATF wind tunnel at a tunnel dynamic pressure of 26.74 psf. Comparisons with CFD were accomplished using a time-accurate Navier-Stokes code. The results show that the air vehicle has two flow structures: an apex and wing vortex. Of the two, the wing vortex appears to be much stronger. The apex vortex exhibited little dynamic frequency content while the wing vortex exhibited a broad band frequency with a range of Strouhal number from 6 to 11. CFD was found to predict the flow field quite well but had difficulty in predicting the dynamic frequency content. Future directions for vehicle control will be focused on wing vortex manipulation through the use of micro-vortex generators or fences.

REFERENCES
1. Kulfan, R.M., "Wing Airfoil Shape Effects on the Development of Leading Edge Vortices," AIAA Paper 79 1675, Reno, NV, January 1979.

2. Billman, G.M., Osborne, B.A., "High L/D Extended Range/Payload Fighter Aircraft Technology," AFRL VA-WP-TR-1999-3084, November 1998.

3. Washburn, A.E., Jenkins, L.N., and Ferman, M.A., "Experimental Investigation of Vortex-Fin Interaction," AIAA 31st Aerospace Sciences Meeting and Exhibit, AIAA 93-0050, Reno, NV, January 1993.

4. Bendat, J.S., and Piersol, A.G., *Engineering Applications of Correlation and Spectral Analysis,* Wiley Publishing, 1980.

5. Welch, P.D., "The Use of Fast Fourier Transform for the Estimation of Power Spectra: A Method Based on Time Averaging Over Short, Modified Periodograms," *IEEE Trans. Audio Electroacoust.*, Vol. AU-15, June 1967.

6. Strang, W.Z., "Parallel Cobalt User's Manual," AFRL, CFD Research Branch Report, Wright-Patterson AFB, OH, September 1999.

7. Strang, William Z., Tomaro, Robert F., Grismer, Matthew J.,"The Defining Methods of Cobalt$_{60}$: A Parallel, Implicit, Unstructured Euler/Navier-Stokes Flow Solver," AIAA Paper 99-0786, January 1999.

8. Rae, W.H., Pope, A. Low-Speed Wind Tunnel Testing, 2nd Edition, Wiley, New York, 1984.

Fig. 8- CFD Flow Visualization
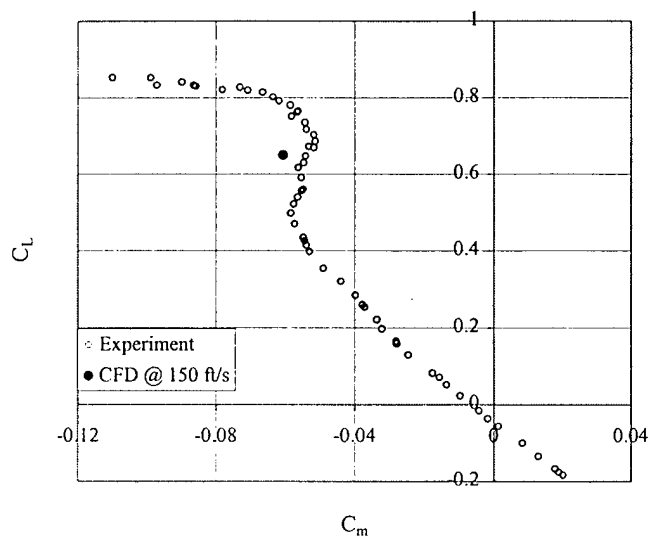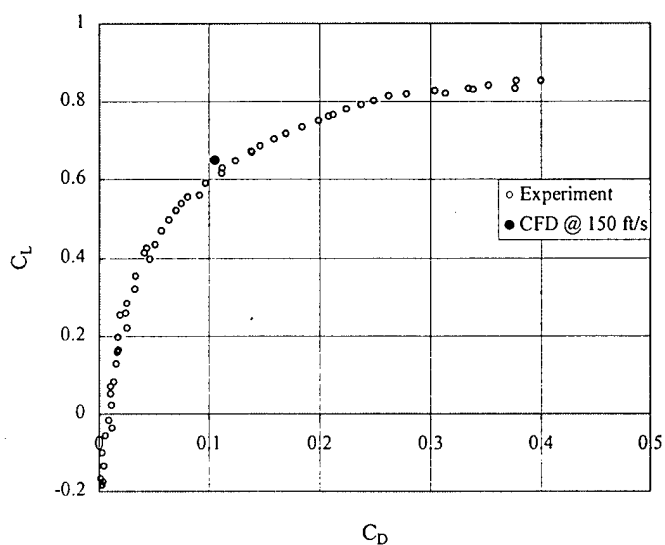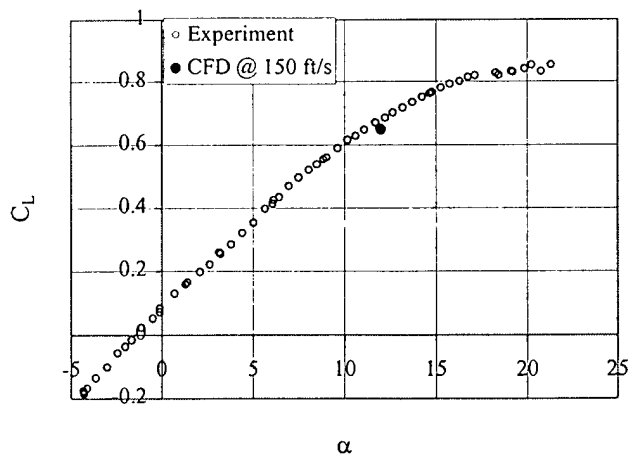
Fig. 7 – Force and Moment Data, a) C_L vs. α,
b) C_L vs. C_D, c) C_L vs. C_m
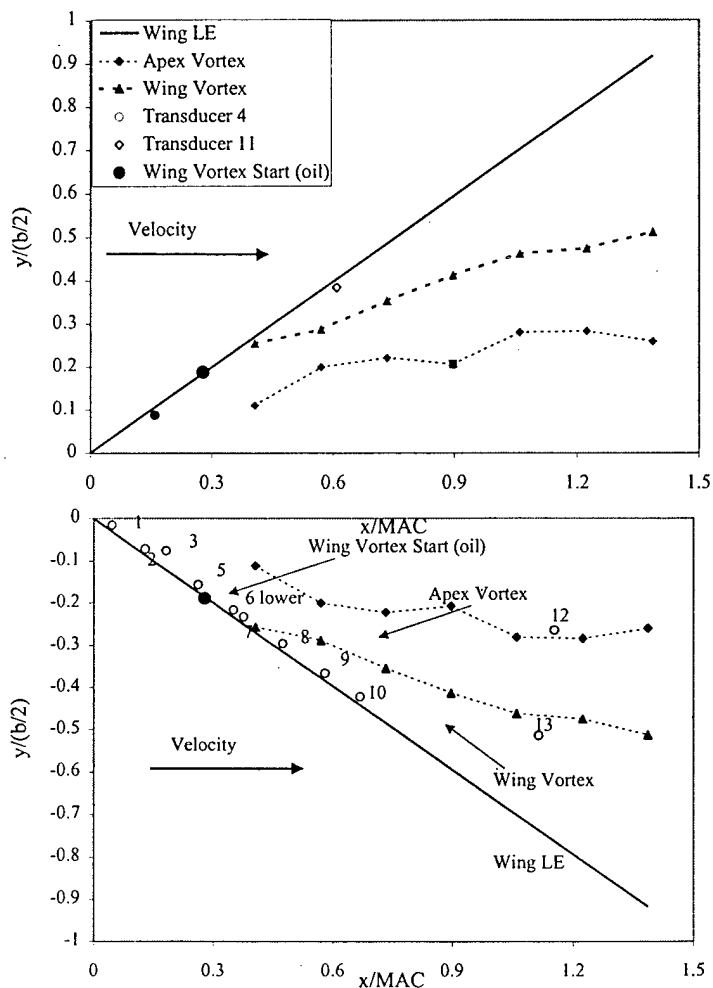
Fig. 9 - a) Starboard Wing, b) Port Wing
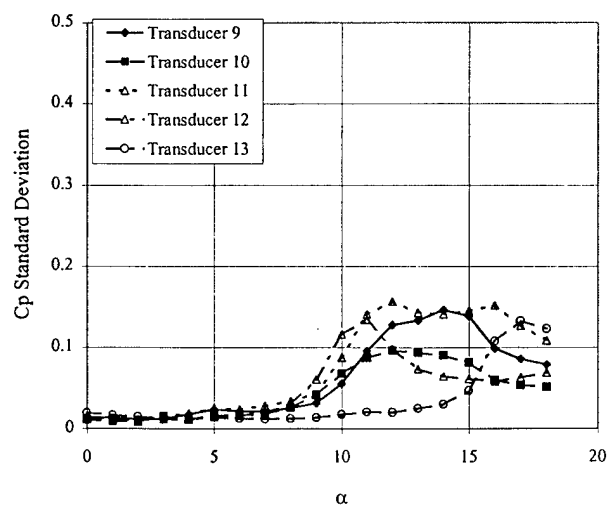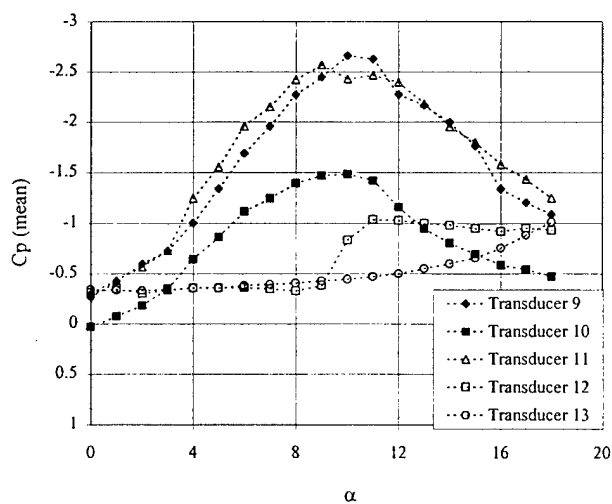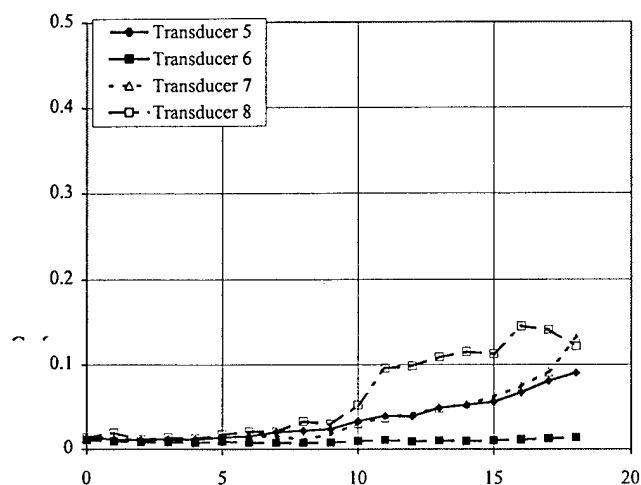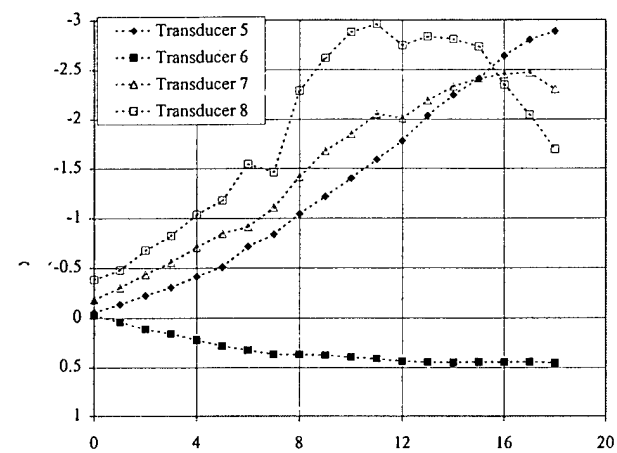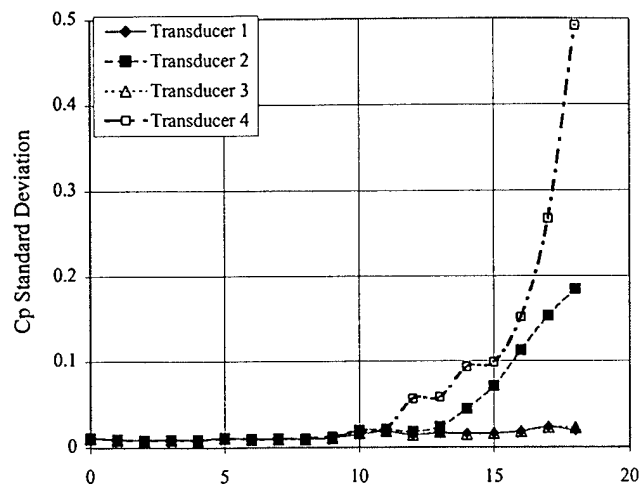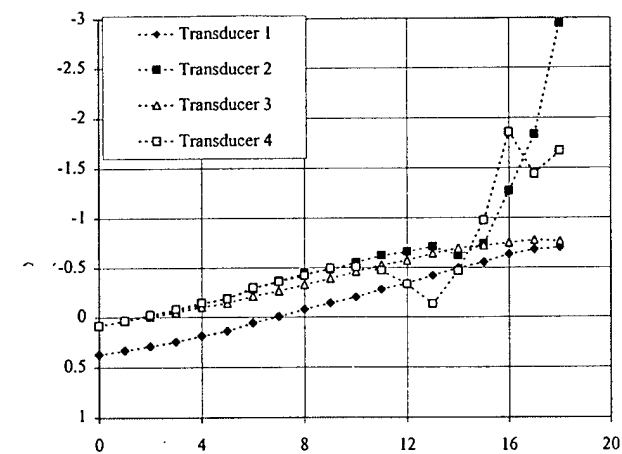
Fig. 10 – Mean Pressure vs. Angle-of-Attack, Unsteady Pressure Data

Fig. 11 – Standard Deviation of Pressure vs. Angle-of-Attack, Unsteady Pressure Data
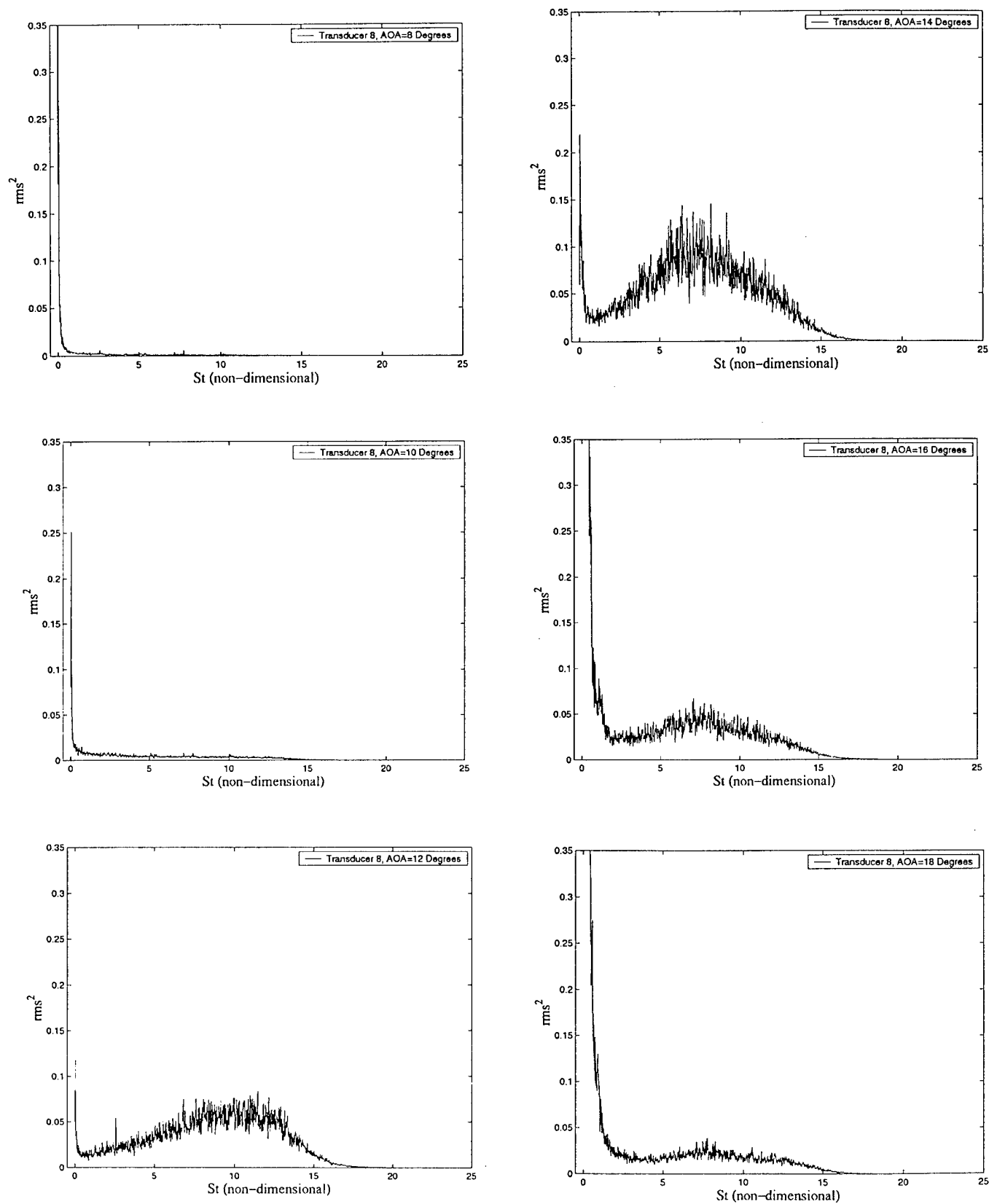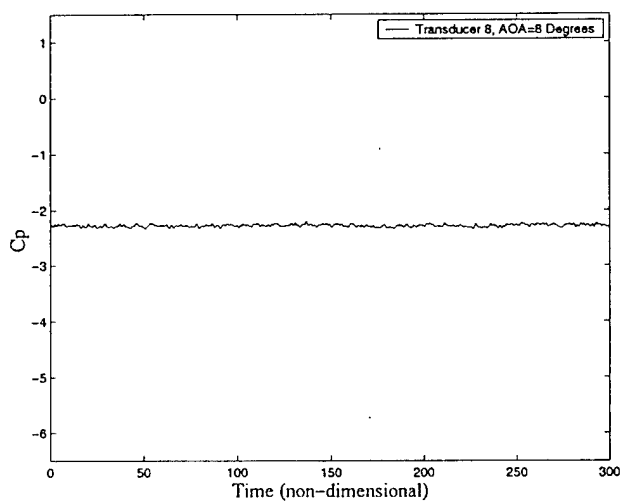
Fig. 12 – PSD For Transducer 8, Increasing Angle-of-Attack
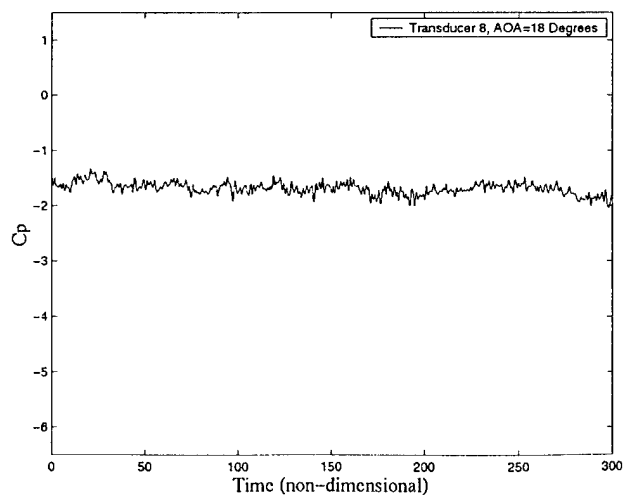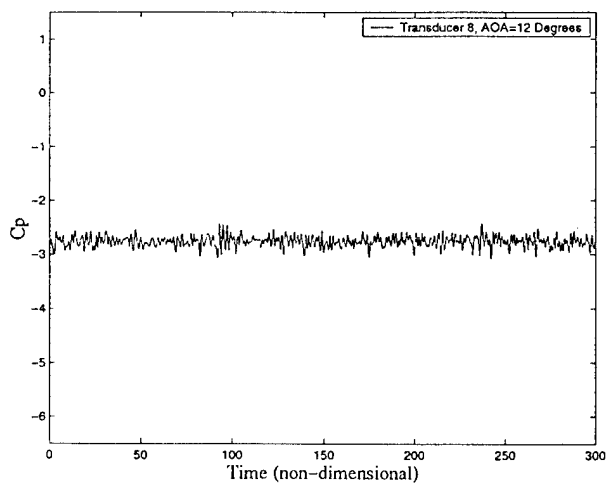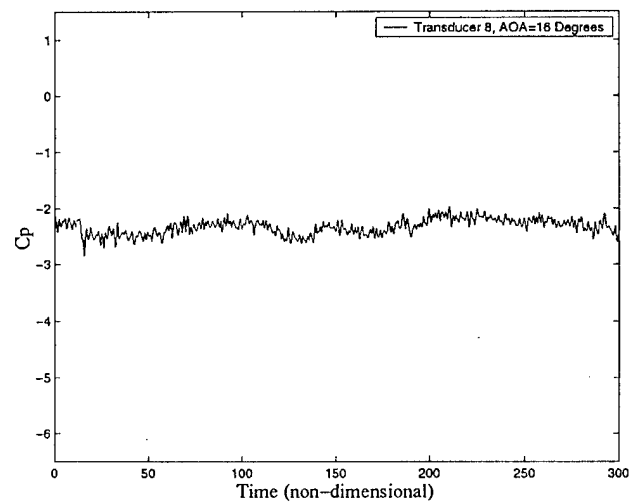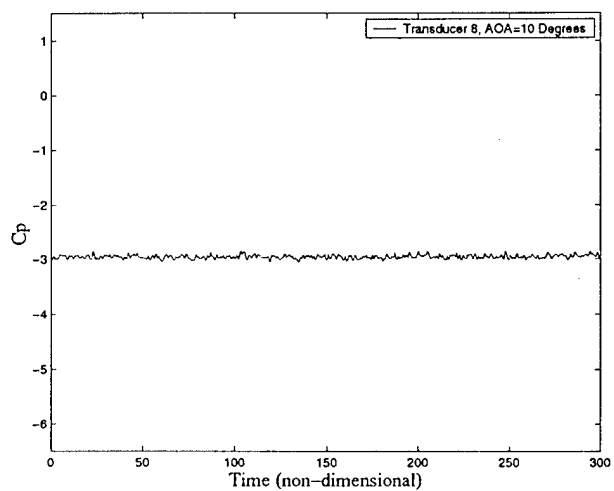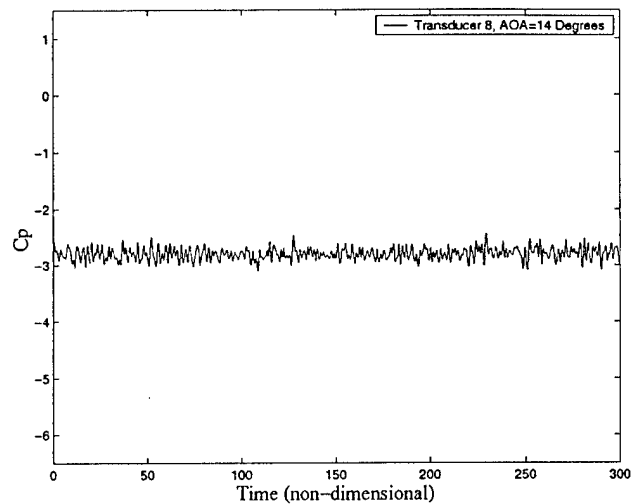
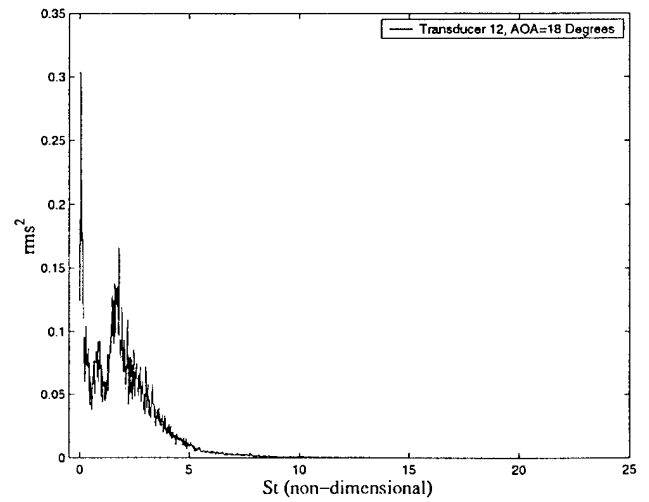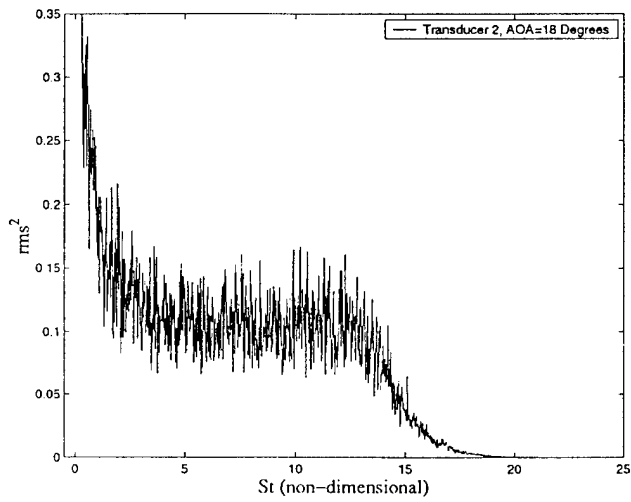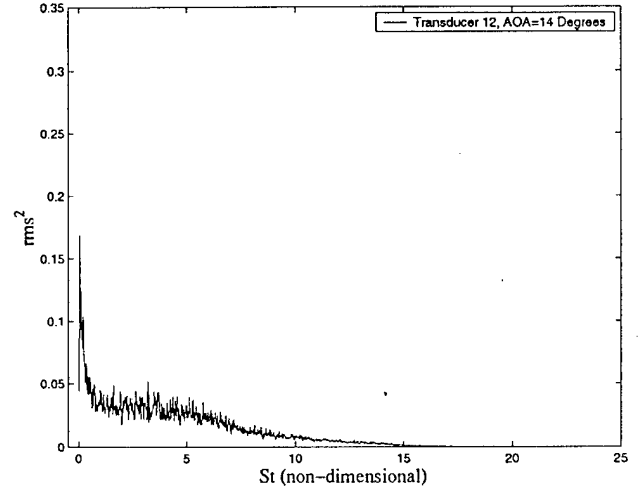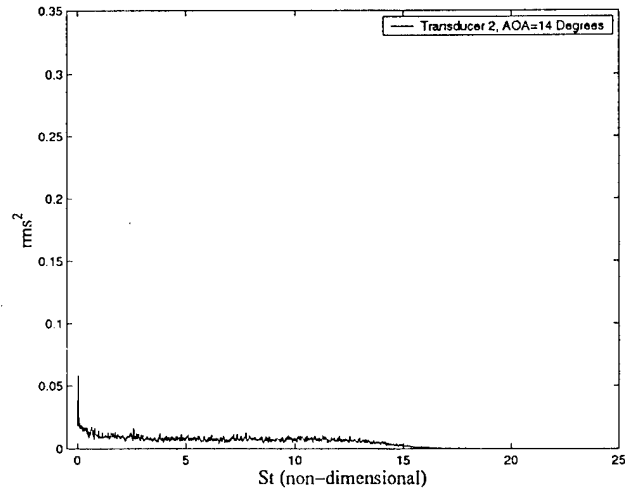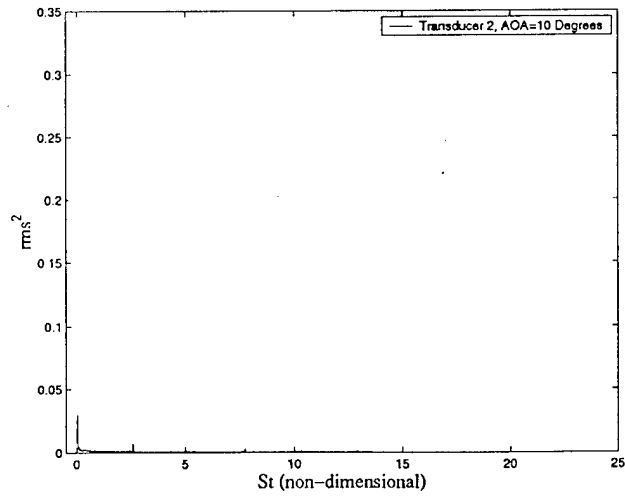Fig. 13 – Time History For Transducer 8, Increasing Angle-of-Attack
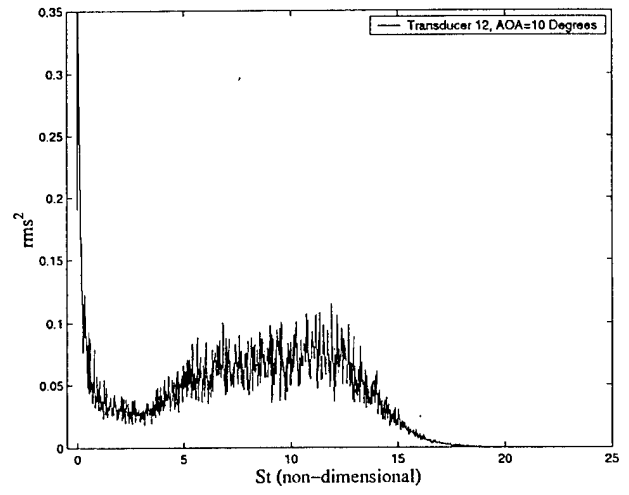
Fig. 14 – PSD for Transducer 2 and 12, Increasing Angle-of-Attack
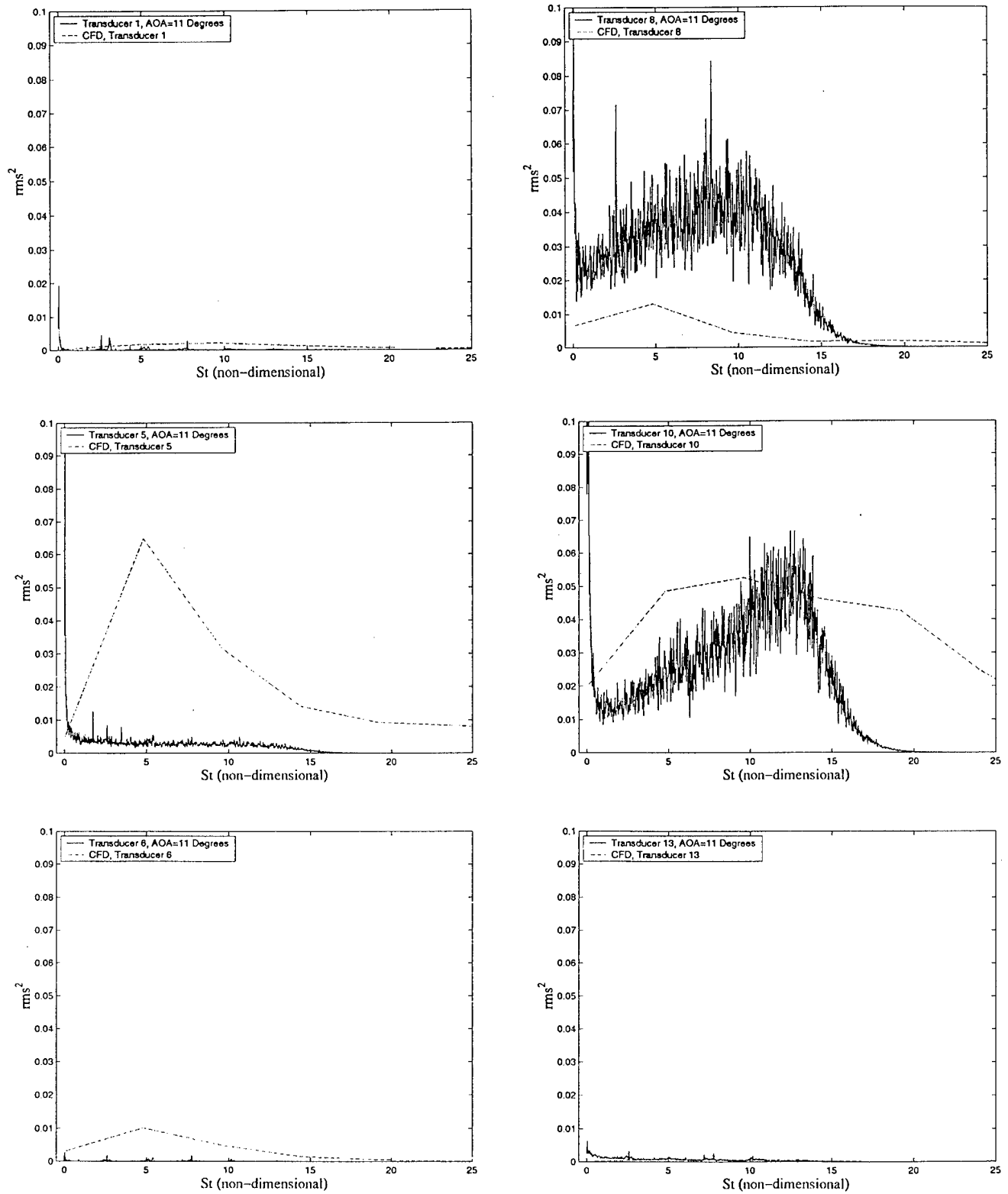
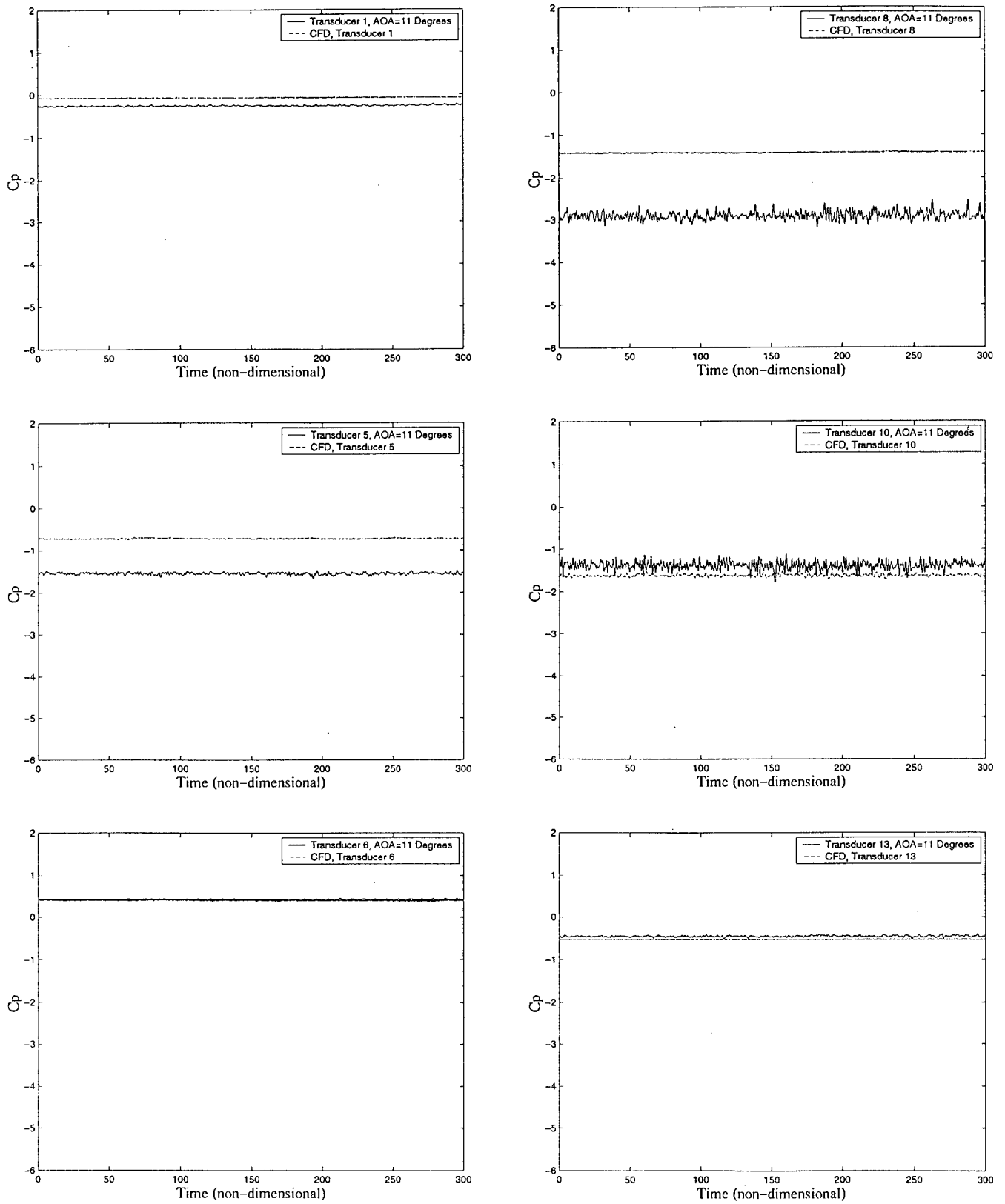Fig. 15 – CFD Comparison to Selected Experimental Data, PSD

Fig. 16 – CFD Comparison to Selected Experimental Data, Time History